Full instantaneous de-icing using extensional modes: The role of architectured and multilayered materials in modes decoupling

G. Gastaldo, M. Budinger, Y. Rafik, V. Pommier-Budinger, V. Palanque, A. Yaich

To cite this version:

G. Gastaldo, M. Budinger, Y. Rafik, V. Pommier-Budinger, V. Palanque, et al.. Full instantaneous de-icing using extensional modes: The role of architectured and multilayered materials in modes decoupling. Ultrasonics, 2024, 138, pp.107264. 10.1016/j.ultras.2024.107264 . hal-04668017v2

Full instantaneous de-icing using extensional modes: the role of architectured and multilayered materials in modes decoupling

G. Gastaldo[a,*], M. Budinger[b], Y. Rafik[b], V. Pommier-Budinger[a], V. Palanque[a], A. Yaich[b]

[a] *Fédération ENAC ISAE-SUPAERO ONERA, University of Toulouse, 31400 Toulouse, France*
[b] *Institut Clément Ader (ICA), University of Toulouse, INSA, ISAE-SUPAERO, MINES ALBI, UPS, CNRS, 31055 Toulouse, France*

Abstract

Ultrasonic de-icing systems are energy-efficient solutions for ice protection. The systems generate high levels of stress in the ice by inducing vibrations in the substrate, resulting in bulk or adhesive ice failure and, ultimately, ice removal. For this purpose, two types of resonant modes can be excited: flexural and extensional modes. The extensional modes have the interesting ability to de-ice substantial areas of the underlying surface as long as they are pure and do not interfere with the flexural modes. However, the coupling between extensional and flexural modes occurs naturally for thin ice-covered substrates. The inertial effect that explains this coupling is demonstrated in this paper by means of the Euler-Lagrange approach. The Euler-Lagrange model also shows how the inertial effect can be eliminated by carefully adjusting the ratio of Young's modulus to substrate density to be close to that of ice. Fi-

---

[*] e-mail address: giulia.gastaldo@isae-supaero.fr

nally, the paper details how multilayered or architectured materials can be used to design piezoelectric plate-like structures to achieve pure extensional modes for de-icing. The ultrasonic de-icing capabilities are demonstrated on prototypes covered with freezer ice.

Keywords: Ultrasonic de-icing, extensional modes, ice fracture, inertial coupling, architectured material

Nomenclature

ϵ	Piezoelectric relative dielectric constants
ν	Poisson's ratio
ω	Angular frequency $[\frac{rad}{s}]$
ϕ	Rotation angle [rad]
ρ	Density $[\frac{kg}{m^3}]$
σ	Stress [Pa]
ε	Strain
E_p	Potential energy [J]
K_i	Key Performance Indicators
k_y	First moment of area $[m^3]$
q_c	Charge $[C]$
A	Beam area $[m^2]$
c	Piezoelectric stiffness coefficients $[\frac{N}{m^2}]$
e	Piezoelectric stress coefficients $[\frac{N}{Vm}]$
I	Second moment of area $[m^4]$
K	Stiffness $[\frac{N}{m}]$

L	Lagrangian function [J]
M	Mass [kg]
T	Kinetic energy [J]
$U(x,t)$	In-plane displacement [m]
$V(x,t)$	Out-of-plane displacement [m]
a	Crack length [m]
b	Width [m]
E	Young's Modulus [Pa]
F	Force [N]
f	Frequency [Hz]
G	Energy release rate [$\frac{J}{m^2}$]
h	Thickness [m]
L	Length [m]
M	Mass [kg]
PFR	Parasitic Flexural Ratio
PZT	Lead zirconate titanate
S	Ice-Substrate contact surface [m^2]

X	In-plane displacement [m]
Z	Out-of-plane displacement [m]

1. Introduction

Icing is a significant problem for wind turbines [1], energy infrastructure (e.g. power lines [2]), and aviation [3]. This phenomenon causes performance losses and affects the reliability of these systems.

Among the negative effects caused by ice accretion on wind turbines, the most relevant are the measurement errors in the wind assessment phase and the power losses [4]. For what concerns aircraft, the accreted ice changes the wing's aerodynamic properties, leading to severe performance degradation and safety hazards [5, 6]. In addition, ice build-up on air intake protection grids leads to increased fuel consumption and power losses [7].

Ice protection systems are therefore necessary to ensure safe and efficient operations. Thermal systems, which heat the exposed surfaces, are the most commonly used solutions for wind turbines and aircraft. They may involve blowing hot air onto the structure or incorporating electrical heating elements to generate a liquid water film [4, 8] at the ice/substrate interface, resulting in the ice shedding under aerodynamic forces. These systems can either prevent ice formation or provide a solution when ice has already accumulated on the structure. The main disadvantage of thermal systems is the high power required to ensure ice protection. Thermal methods have also been adapted and used for de-icing electrical power lines. An overview of the main thermal techniques is given by Laforte et al. [2]. They involve either heating the conductors by the Joule Effect or indirect heating through resistive wires or a ferromagnetic envelope. Again, these systems require high energy levels, between 1 and 10 kW/m^2 ([2]).

Mechanical de-icing systems are less energy-demanding solutions. They create significant stresses in the ice, leading to its failure and eventual ice shedding. Pneumatic systems are low-energy solutions used on regional and smaller aircraft. When sufficient ice accumulates, pulses of compressed air inflate and deflate the pneumatic boots. Unfortunately, they significantly impact the aircraft's aerodynamics and require regular maintenance due to the limited durability of the boot material [9, 10]. Alternative mechanical systems are studied to limit the required power supply. In recent years, vibratory and ultrasonic de-icing systems have attracted increasing interest due to their potential weight and energy savings. This type of system may be particularly beneficial for certain aircraft configurations, such as commuter and regional aircraft, where the available power is insufficient for thermal ice protection systems.

1.1. Vibratory and ultrasonic de-icing

Vibratory de-icing is based on electromechanical systems that excite the surface covered with ice with vibrations that generate high stresses in the ice, leading to its fracture and ultimately to its removal [11, 12]. The most studied electromechanical systems for vibratory de-icing are based on piezoelectric actuators. In [12], the authors found that a low-energy piezoelectric actuated system can be used to de-ice a rotorcraft blade. De-icing was accomplished by exciting multiple resonant frequencies through a frequency sweep, which caused the ice to crack and debond at multiple locations. Venna et al. [13] attempted to achieve electromechanical de-icing of a leading edge using a frequency range of approximately 1 kHz. They used finite element analysis to calculate the magnitude of vibration required to exceed the shear strength of the interface. The ice detachment was achieved after exciting the structure for 60 to 120 seconds. This may be due to heating effects. In [14], Villeneuve et al. triggered fracture and debonding in a large plate covered with a narrow ice layer, representative of ice accumulation on a leading edge. Numerical simulations were used to identify the resonant modes that could cause cracking or delamination of the ice, and the results were validated experimentally.

Ultrasonic de-icing is a type of vibratory de-icing that uses frequencies in the kilohertz range. Its applicability on wind turbine blades, high voltage transmission lines, and aircraft is reviewed in detail in [15]. It was first proposed by Ramanathan et al. [16], who used piezoelectric actuators in a range of frequencies around 1 MHz for helicopter blade de-icing. When high-energy ultrasonic waves pass through a plate-ice layered system, the shear stresses at the interface are high enough to detach the ice layer from the structure. In this paper, however, the de-icing was due to a combination of heating and mechanical effects caused by ultrasonic vibrations. In [17], ultrasonic de-icing was applied to composite wind turbine blades using frequencies around 360 kHz. In the experimental results, the required de-icing time varied between 30 s and 300 s, depending on the ice thickness. However, it is worth considering that the duration of the experiment may have resulted in some thermal effects during the mechanical de-icing process. With more success, Palacios et al. conducted a study on de-icing systems using ultrasonic frequencies of 28 to 32 kHz on both plates and leading edges, which resulted in instantaneous de-icing [18, 19]. Under the influence of ultrasonic excitation, rotor icing tests were performed by Overmeyer et al.[20], which also led to immediate ice detachment. Li and Chen [21] conducted the study on ultrasonic de-icing of vertical surfaces and observed that the accumulated small samples of ice are also shed instantly.

In [22], two types of resonant modes that can be adopted for electromechanical de-icing are evaluated: flexural modes, characterized by a significant out-of-plane displacement, and extensional modes, which vibrate mainly in the in-plane direction. The first should be chosen if low power consumption is required, knowing that the area that can be protected is limited. Contrarily, extensional modes require higher power [23], but they are more suitable for completely de-icing the surfaces to be protected. Although the extensional modes consume more power than the flexural ones, the power consumption of resonant de-icing systems based on this kind of mode is still competitive when compared to thermal de-icing systems. Power calculations for an A320 aircraft showed that an electromechanical de-icing system based on extensional modes consumes 2.0 kVA/m^2. In contrast, an electrothermal de-icing system consumes approximately 4 kVA/m^2 and an electrothermal anti-icing system requires approximately 20 kVA/m^2 [24]. In addition, the study found that the power consumption of electromechanical de-icing could be further reduced by optimizing activation times, as conservative times were used for the de-icing cycles. Therefore, although the extensional modes consume more power than the flexural modes, the power consumption of resonant de-icing systems based on extensional modes is still competitive compared with other de-icing technologies.

However, it is not always possible to obtain pure extensional modes. For example, in a multi-layered structure with heterogeneous material properties, such as an iced structure, the pure extensional mode may be coupled to and parasitized with a flexural mode. Exciting a coupled extensional mode that is not pure would reduce the effectiveness of de-icing, as the undesired flexural motion would trigger the corresponding ice failure mechanism, resulting in a smaller protected area.

This work investigates the coupling between flexural and extensional modes and establishes an effective decoupling methodology. Section 2 quantifies the negative effects of the coupling between extensional and flexural modes during de-icing based on extensional modes. In section 3, the coupling is modeled using an analytical approach based on the Euler-Lagrange equations. The final sections of the paper propose a method to decrease or eliminate the coupling by modifying the substrate properties using multi-layered materials.

2. Effects of parasitic flexion on de-icing with an extensional mode

2.1. De-icing mechanisms

Electromechanical de-icing systems are designed to create stresses within the ice to initiate and propagate fractures. According to the fracture mechanics theory, two types of fractures can be considered: cohesive and adhesive fractures. The former occurs in the ice bulk, while the latter appears at the interface (see figure 1). Budinger et al. [25] studied the fracture propagation following its initiation and presented two de-icing mechanisms: one induced by tensile stress and the other by shear stress. In the first mechanism, the cohesive fracture occurs within the ice thickness when the tensile stress in the ice exceeds its tensile strength (1 to 3 MPa, depending on the type of ice [26], [27]). After the cohesive crack is generated, the interface undergoes delamination due to the exceeded critical energy release rate. The second mechanism involves the initiation and propagation of the adhesive fracture, which occurs when the shear stress at the interface exceeds its shear strength. Villeneuve et al. [14, 28] later confirmed the stress-related fracture mechanisms for both steel plates and helicopter blades. As shown in [29], for a plate entirely covered with ice and vibrating in the first extensional mode, cohesive cracks will appear first, followed by adhesive delamination, which corresponds to the first mechanism.

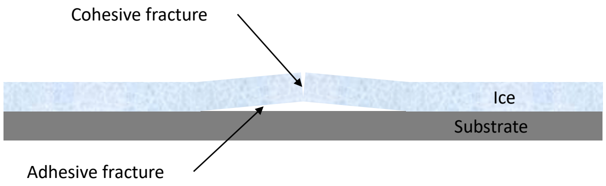

Figure 1: Ice fracture mechanisms: cohesive and adhesive fractures.

2.2. Performance indicators for resonant de-icing systems

The efficiency of a de-icing system is usually determined by its ability to propagate an adhesive fracture. As previously stated, a de-icing system is considered efficient if it generates either sufficient energy release rate G or stress σ levels to initiate and propagate the fracture throughout the entire interface. It is important to note that the energy release rate G can be defined as follows:

$$G = -\frac{1}{b}\frac{dE_p}{da} \tag{1}$$

where dE_p is the differential decrease in potential energy, da is the differential increase in crack length, and b is the specimen width.

The energy release rate G depends on the vibratory amplitude X and the potential energy U of the deformed structure. In [23], a set of Key Performance Indicators (KPI) was proposed to make the analyses independent of the vibratory amplitude. In equation 2, 3, two of these indicators are reported. K_σ represents the system's ability to propagate fractures for a given stress level, while K_U relates to the operating limits of the actuation system in terms of energy.

$$K_\sigma = \frac{G}{\sigma^2} \tag{2}$$

$$K_U = \frac{G}{U} \tag{3}$$

The results obtained with the K_σ and K_U indicators have shown that adhesive fractures following the cohesive fractures will be greater in the case of extensional modes when a plate-like structure is considered [23]. In particular, the K_U indicator showed that the delamination performances of an extensional mode are maintained over a much larger area than those of the flexural mode, allowing a fracture length greater than 80%. Therefore, extensional modes seem to be the most suitable solution if the detachment of large portions of ice is desired.

2.3. Effect of parasitic flexural modes

The indicators presented were determined for a homogeneous 1 mm-thick titanium plate with a 2 mm-thick layer of ice on top. In this configuration, the computations were performed assuming that the flexural and extensional resonant modes were pure and uncoupled. However, the accumulated ice may have different mechanical properties and geometries than the structure it adheres to. This can result in parasitic flexion, even in simple structures such as plates. Moreover, in the aeronautic field, the structures exposed to ice have complex geometries, which leads to even more pollution of the extensional modes by parasitic flexural ones.

This study aims to investigate the impact of this parasitic flexion on the effectiveness of de-icing through extensional resonant modes. To this end, a structure covered with ice is studied. Only a quarter of the geometry is studied to reduce the computing time. To generate parasitic flexion, a block is added at the plate's end (figure 2(a)). The greater its thickness (and mass), the more the neutral line is displaced. As a result, the extensional mode is disturbed by parasitic flexion. Table 1 presents, for blocks of different thicknesses and masses, the parasitic flexural ratio defined as the ratio between the maximum normal (out-of-plane) displacement Y and the maximum tangential (in-plane) displacement X. Computations were run for the first extensional mode.

Table 1: Parasitic flexural ratio for different block thicknesses

Block Thickness [mm]	0	0.5	1	2.5	5	10
Parasitic flexural ratio	0.05	0.07	0.11	0.038	0.82	1.02

The K_X indicator is introduced. It represents the system's ability to propagate fractures for a given in-plane displacement X, thus for an extensional mode. It can be expressed as follows:

$$K_X = \frac{G}{X^2} \tag{4}$$

The K_X indicator is computed for the homogeneous 1 mm-thick titanium plate with a 2 mm-thick layer of ice on top and for the first extensional mode with the different ratios of parasitic flexion of Table 1. It is computed by integrating the energy stored in the ice relative to different areas. To this end, the ice is divided into 20 sections of surface S, each representing 5% of the interfacial length that may be subject to adhesive failure. Therefore, a K_{X_i} indicator for each ice segment i can be defined as follows:

$$K_{Xi} = \frac{1}{X^2}.\frac{E_{pi}}{S} \tag{5}$$

where X is the maximum in-plane displacement of the structure, E_{pi} the energy stored in each block i and S the ice block-substrate contact surface.

This approach makes it possible to calculate and plot the evolution of K_X for each block according to its position along the length of the plate (Figure 2(b)).

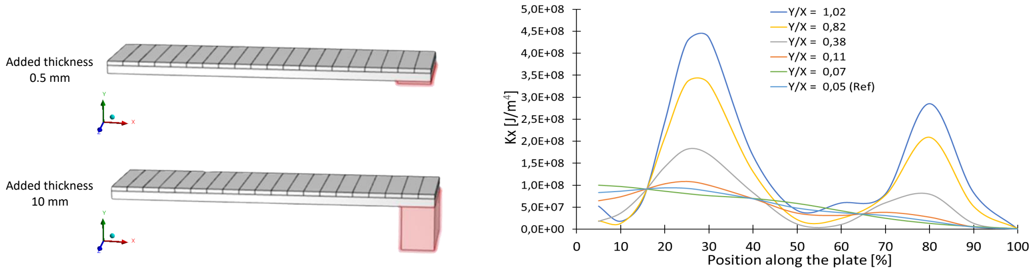

(a) (b)

Figure 2: Parasitic flexural ratio effect: (a) titanium plate with ice accumulated on top with a local mass added to generate parasitic flexion (b) K_X indicator as a function of the position along the plate.

The K_X indicator of the structure with no added mass is represented by the light blue curve. In this case, the extensional mode has minimal flexural interference (as quantified by the ratio $\frac{Y}{X} = 0.05$) and the curve exhibits a smooth trend. However, as the deformation of the extensional mode is affected by flexion, the trend of the K_X curve experiences peaks of increasing amplitudes for higher parasitic flexural ratios. In figure 2(b), it is possible to notice that the position of the peaks corresponds to the location of the antinodes (points of maximum displacement) of the parasitic flexural mode. These non-uniform trends of the K_X indicator may induce propagation on a restricted portion of the structure while producing an adverse impact in some other areas (as depicted in figure 2(b), typically in the range from 0% to 15% and from around 50% to 70% of the plate's half-length). In these areas, the propagation is expected to stop due to the sharp decrease in the indicator. For this reason, a uniform trend of the pure extensional mode is desired.

Therefore, to ensure complete adhesive detachment of the ice layer, this study will focus on designing prototypes that maintain the ratio of parasitic flexion $\frac{Y}{X}$ below a value of 0.4.

3. Analytical investigation of the coupling of flexural and extensional resonant modes

This section aims to investigate the origin of the coupling between extensional and flexural modes. For this purpose, it is essential to study the analytical wave equations of the system. Hereafter, the study is carried out for an oscillating beam in free boundary conditions. The equations are obtained from the Euler-Lagrange formulation of the problem.

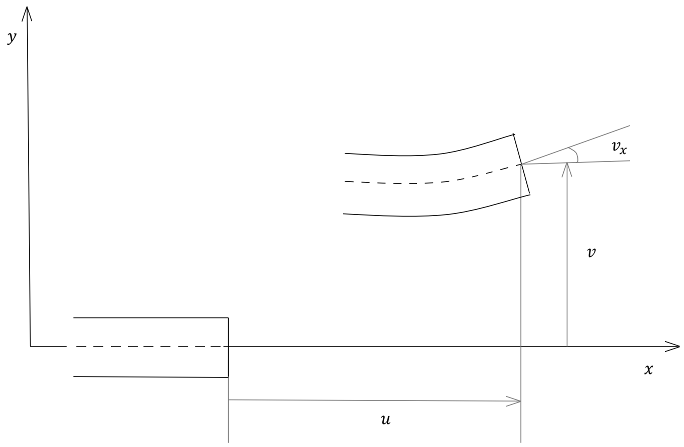

Figure 3: Undeformed and deformed beam.

3.1. Coupled wave equations from the Euler-Lagrange formulation

Consider a portion of the beam subject to both extension and flexion, as seen in figure 3, x being the position along the beam and y the position relative to the beam neutral axis. For a homogeneous beam, the neutral axis lies on the centerline, but if a multi-material beam is considered the neutral axis position is dependent on the material properties and the different thicknesses.

The in-plane and out-of-plane displacements $U(x,t)$ and $V(x,t)$ are defined as follows[1] :

---

[1] To simplify the writing of equations, this paper will use the following notations for the first and second derivatives: $\frac{\partial f}{\partial x} = f_x$ and $\frac{\partial^2 f}{\partial x \partial y} = f_{xy}$, and for the time derivative $\frac{\partial f}{\partial t} = f_t$

$$U(x,t) = u(x,t) + y\phi(x,t) = u(x,t) - yv_x \tag{6}$$

$$V(x,t) = v(x,t) \tag{7}$$

where $u(x,t)$ and $v(x,t)$ are respectively the in-plane and out-of-plane displacement components of the neutral axis, and $\phi(x,t)$ is its rotation expressed as $\phi = -\frac{\partial v}{\partial x} = -v_x$ and obtained from the assumption of shear stress $\gamma_{xy} = u_y + v_x = 0$.

As previously mentioned, the goal is to obtain the wave equations using the Euler-Lagrange formulation based on the Lagrangian function defined by:

$$L(x,t) = T - E_p \tag{8}$$

where T is the system kinetic energy and E_p is its potential energy. They are defined as:

$$T = \int \frac{1}{2}(U_t^2 + V_t^2)dm = \iint \frac{1}{2}\rho(U_t^2 + V_t^2)dSdx \tag{9}$$

$$E_p = \int \frac{1}{2}E\varepsilon^2 dV = \iint \frac{1}{2}E\varepsilon^2 dSdx \tag{10}$$

By substituting $U_t^2 + V_t^2$ into the kinetic energy expression 9, the following equation is obtained:

$$T = \int \left[\frac{1}{2}(\rho A)_{eq}(u_t^2 + v_t^2) - (\rho k_y)_{eq} u_t v_{xt} + \frac{1}{2}(\rho I)_{eq} v_{xt}^2 \right] dx \tag{11}$$

with $(\rho A)_{eq} = \int \rho(y) dS$, $(\rho k_y)_{eq} = \int \rho(y) y dS$, $(\rho I)_{eq} = \int \rho(y) y^2 dS$. In the case of a structure covered with ice, the density ρ and Young's modulus E depend on the position relative to the neutral axis y. This possible distribution explains the notation $\rho(y)$ and $E(y)$. Also, the notation $()_{eq}$ is used to express the equivalent contributions that can be obtained for a multi-material system.

In the case of a slender beam, the kinetic energy of rotation can be neglected, thus giving the final expression:

$$T = \int \left[\frac{1}{2}(\rho A)_{eq}(u_t^2 + v_t^2) - (\rho k_y)_{eq} u_t v_{xt} \right] dx \tag{12}$$

Knowing that $\varepsilon = u_x - y\phi_x$, the potential energy can be expressed as follows:

$$E_p = \iiint \left[\frac{1}{2} E(y)(u_x - y\phi_x)^2 \right] dS dx = \int \left[\frac{1}{2}(EA)_{eq} u_x^2 - (Ek_y)_{eq} u_x v_{xx} + \frac{1}{2}(EI)_{eq} v_{xx}^2 \right] dx \tag{13}$$

with $(EA)_{eq} = \int E(y) dS$, $(Ek_y)_{eq} = \int E(y) y dS$, $(EI)_{eq} = \int E(y) y^2 dS$. The term $(Ek_y)_{eq} = \int E(y) y dS = 0$ by definition of the neutral axis.

Equation 8 can be now written as:

$$L(x,t) = T - E_p = \int L_x dx = \int \Big[\frac{1}{2}(\rho A)_{eq}(u_t^2 + v_t^2) - (\rho k_y)_{eq} u_t v_{xt} - \frac{1}{2}(EA)_{eq} u_x^2 - \frac{1}{2}(EI)_{eq} v_{xx}^2 \Big] dx \tag{14}$$

By minimizing the Lagrangian (equation 8), it is possible to obtain the following system of equations:

$$\frac{d}{dx}\frac{\partial L_x}{\partial u_x} + \frac{d}{dt}\frac{\partial L_x}{\partial u_t} = 0 \tag{15a}$$

$$\frac{d^2}{dx^2}\frac{\partial L_x}{\partial v_{xx}} - \frac{d}{dt}\frac{\partial L_x}{\partial v_t} + \frac{d^2}{dxdt}\frac{\partial L_x}{\partial v_{xt}} = 0 \tag{15b}$$

Substituting L_x in the system of equations 15 leads to the following set of equations:

$$(\rho A)_{eq}\frac{\partial^2 u}{\partial t^2} - (\rho k_y)_{eq}\frac{\partial^3 v}{\partial x \partial t^2} - (EA)_{eq}\frac{\partial^2 u}{\partial x^2} = 0 \tag{16a}$$

$$(\rho A)_{eq}\frac{\partial^2 v}{\partial t^2} + (\rho k_y)_{eq}\frac{\partial^3 u}{\partial x \partial t^2} + (EI)_{eq}\frac{\partial^4 v}{\partial x^4} = 0 \tag{16b}$$

It is possible to notice that the two equations are not independent. They are coupled by the term $(\rho k_y)_{eq} = \int \rho(y) y dS$, which provides information on the inertial coupling of the system. In the case of a homogeneous beam, this term is equal to zero since y is the position relative to the neutral axis. The two equations become the equations of free motion for a beam in extension and a bending beam.

For a multi-material beam, the two equations are coupled, thus leading to the presence of parasitic flexion when an extensional mode is excited. If the ratio $\frac{E(y)}{\rho(y)}$ does not vary from one layer to the other, the inertial coupling term is equal to zero by definition of the neutral axis ($\int E(y) y dS = 0$).

The results of the analytical model are verified by means of numerical analyses. Two 2D numerical analyses are performed on a beam with a 2.5 mm layer of ice accreted on top. The ice properties are those of glaze (or freezer) ice ($E = 9$ GPa, $\rho = 900$ kg/m^3). In the first case, the beam is made of a titanium alloy (TA6V), while in the second case, the beam is made of a fictitious material having a ratio $\frac{E}{\rho}$ equal to the one of ice. It is possible to notice in figure 4 that when an extensional mode is excited, the titanium beam oscillates with a coupled extensional/flexural mode, whereas the fictitious beam presents a pure extensional mode.

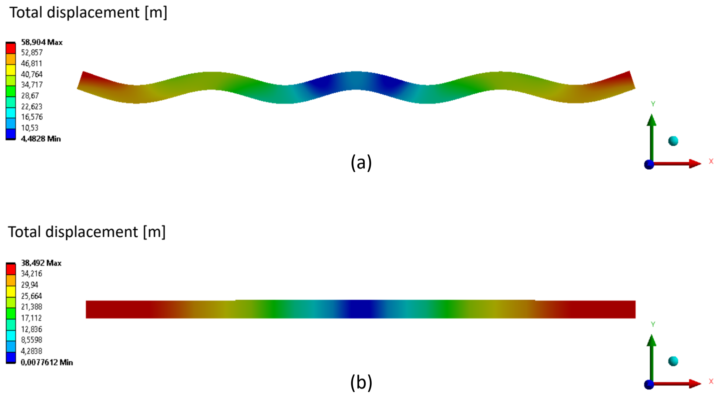

Figure 4: 2D extensional mode for two different beams with 2.5 mm of ice accreted on top: (a) the beam is constituted by a titanium alloy, having an $\frac{E}{\rho}$ ratio different from that of ice (b) the beam is constituted by a fictitious material having $\frac{E}{\rho}$ equal to that of ice.

3.2. Coupling analysis with a Rayleigh-Ritz based approach

The Rayleigh quotient and the Ritz approach [30] can be used here to approximate the angular frequency ω and analyze the coupling between flexion and extension. The beam is assumed to be subject to pinned-pinned boundary conditions at the edges. The in-plane and out-of-plane displacements can be written as:

$$U(x,t) = U_0 sin(\pi \frac{x}{L}) sin(\omega t) \tag{17}$$

$$V(x,t) = V_0 sin(\pi \frac{nx}{L}) sin(\omega t) \tag{18}$$

where U_0 and V_0 are the maximum amplitudes of the extensional and flexural modes. The expressions 12 and 13 of the maximum elastic and kinetic energies can then be written as:

$$E_p = \frac{L}{4}\Big[EA(\frac{\pi}{L})^2 U_0^2 + EI(\frac{n\pi}{L})^4 V_0^2\Big] \tag{19}$$

$$T = \omega_0^2\Big[\frac{1}{4}\rho AL(U_0^2 + V_0^2) - \rho k_y C_n U_0 V_0\Big] \tag{20}$$

with:

$$C_n = ((-1)^{n+1} - 1)\Big[\frac{n}{(n^2-1)}\Big] \tag{21}$$

The coupling term is nonzero only if n is an even number. The equality of the two energy contributions enables the approximation of the angular frequency:

$$\omega_0^2 = \frac{\frac{L}{4}\Big[EA(\frac{\pi}{L})^2U_0^2 + EI(\frac{n\pi}{L})^4V_0^2\Big]}{\frac{1}{4}\rho AL(U_0^2 + V_0^2) - \rho k_y C_n U_0 V_0} \tag{22}$$

Equation 22 can be written as a function of the parasitic flexural ratio $\alpha = \frac{V_0}{U_0}$:

$$\omega_0^2 = \frac{a\alpha^2 + b}{c\alpha^2 + d\alpha + e} \tag{23}$$

with:

$$\begin{aligned} a &= \tfrac{L}{4}EI(\tfrac{n\pi}{L})^4 \\ b &= \tfrac{L}{4}EA(\tfrac{\pi}{L})^2 \\ c &= e = \tfrac{L}{4}\rho A \\ d &= -\rho k_y C_n \end{aligned} \tag{24}$$

The mode shape is determined by minimizing the angular frequency (equation 22) [30], thus by computing:

$$\frac{\partial \omega_0^2}{\partial \alpha} = 0, \tag{25}$$

which leads to:

$$ad\ \alpha^2 + (2ac - 2bc)\ \alpha - bd = 0 \tag{26}$$

Solving equation 26 allows the computation of the parasitic flexural ratio corresponding to the mode ω_0. Note that this equation shows that there is no flexural/extensional coupling ($\alpha = 0$) if $d = 0$, which corresponds to $\rho k_y = 0$, consistent with the previous section's result.

3.3. Application: a plate-like structure covered with ice

Let us consider a titanium plate with an accumulated ice layer of variable thickness. Table 2 presents the geometrical and material properties of the assembly.

Table 2: Geometry and materials properties

Description	symbol	Substrate	Ice
Length	$L[mm]$	130	130
Thickness	$h[mm]$	1.5	[1;5]
Young's modulus	$E[GPa]$	110	9
Poisson's Ratio	ν	0.3	0.3
Density	$\rho[kg/m^3]$	4370	900

This example aims to identify the configurations that cause excessive parasitic flexion. To this end, the analytical Rayleigh-Ritz approach is used and a FEM analysis is performed to plot the mode shapes and validate the results provided by the analytical method.

Figure 5(a) presents the obtained parasitic flexural ratios versus the ice block thickness using the Rayleigh-Ritz approach for different values of n. It can be seen that two peaks of parasitic flexion occur for $n = 8$ and $n = 6$, respectively, and for ice thicknesses h_{ice}= 2.1 mm and 3.7 mm. The modal shapes of the coupled extensional modes, which are obtained using FEM numerical analyses, are displayed in figure 5(b). The analytical and numerical methods differ on the value of ice thickness at which the two peaks occur (h_{ice}

= 2.6 mm and 5.1 mm compared to h$_{ice}$= 2.1 mm and 3.71 mm), but they are coherent in both the number of antinodes of the parasitic flexural mode and in the obtained parasitic flexural ratio. Indeed, for $n = 8$, the analytical parasitic flexural ratio is 0.58, while the numerical one is PFR=0.56. For $n = 6$, the analytical value is 0.96, while the numerical PFR is 1.04. Therefore, the analytical method provides a good first approximation to identify the configuration of ice thickness that leads to parasitic bending and to provide a quick estimate of the parasitic bending ratio.

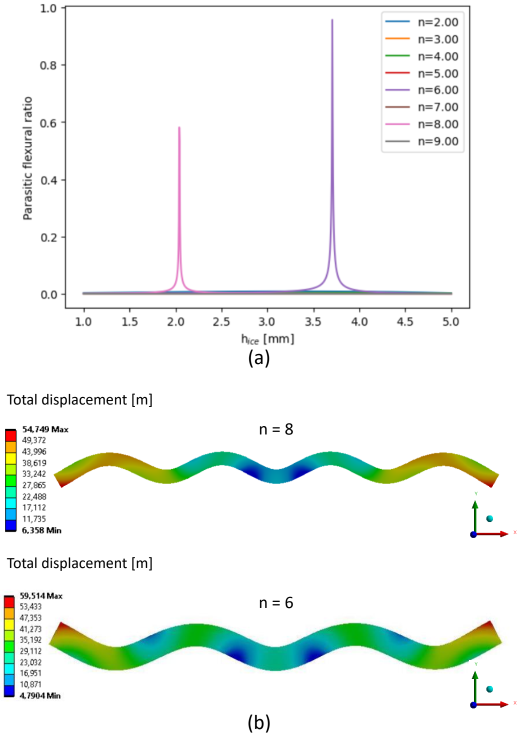

Figure 5: (a) Analytical analysis of parasitic flexion using Rayleigh-Ritz approach. The peaks in parasitic flexion correspond to the superimposition of the flexural mode characterized by n antinodes, which leads to an increase in the parasitic flexural ratio. (b) FEM extensional modes for the first peak ($n = 8$) and the second peak ($n = 6$).

4. Proposal of material and multi-material architectured substrates for instantaneous de-icing

4.1. Selection of materials for multi-material substrates

Since all structures covered by ice behave as non-homogeneous structures, one first option to decouple extensional modes from parasitic flexion is to select the substrates properly.

A map of the materials of interest for selecting a substrate that limits the parasitic flexion by presenting an interesting $\frac{E}{\rho}$ ratio is shown in figure 6. It is possible to notice that a few materials (such as glass fiber reinforced composite, lead, and copper) have $\frac{E}{\rho}$ ratios that closely match that of glaze ice. The figure shows a curve corresponding to the $\frac{E}{\rho}$ ratios of the ice in different states. These ratios are calculated using the results obtained by Palanque et al. [31]. In their article, they determined the values of Young's modulus and density of ice in both a cold chamber and an icing wind tunnel by varying parameters such as temperature, liquid water content, median volume diameter, and wind speed. The rest of the study is conducted on high-density freezer ice to make an initial assessment of the phenomenon.

An evaluation of the relative E/ρ ratio ($(E/\rho)_{substrate}/(E/\rho)_{ice}$) was performed for freezer ice to understand how the choice of the adopted materials would influence the parasitic flexural ratio. Figure 7 presents the parasitic flexural ratio when varying the relative E/ρ ratio for different ice thicknesses. It is possible to define in the graph a non-optimal zone, in which the parasitic flexural ratio reaches high values for some ice thicknesses. An optimal zone

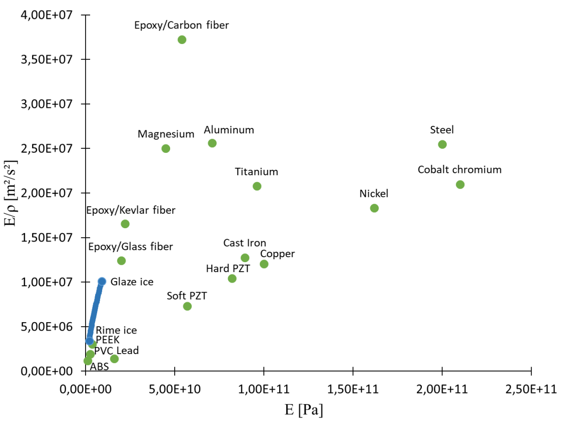

Figure 6: Ratios $\frac{E}{\rho}$ of different materials compared to those of ice.

of the graph can also be defined, where the parasitic flexural ratio remains low regardless of the value of the ice thickness. In this part of the plot, the PFR is limited to a maximum of 0.45. Hence, choosing a material with a relative E/ρ ratio between 1 and 1.45 is beneficial for maintaining a low value of the PFR for any ice thickness and, therefore, for de-icing structures with extensional modes.

Getting a relative E/ρ ratio between 1 and 1.45 is not possible with any type of substrate material. It should be noticed that the relative ratio of E/ρ of titanium and ice is around 2.1. In this case, one option is to create architectured materials to adjust the material properties and get ratios $\frac{E}{\rho}$ equivalent to that of ice. Theoretically, the relative E/rho ratio that ensures parasitic flexural ratios below 0.45 could be less than 1. However, the study was not performed for these values as they are too far from the application case.

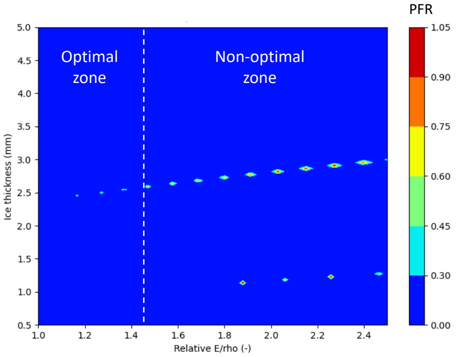

Figure 7: Parasitic flexural ratio function of substrate material properties.

4.2. Architectured materials

Architectured (or hybrid) materials can be defined as a combination of two or more materials and space [32]. They enable a combination of properties not offered by a monolithic material [33]. Examples of architectured materials are particulate and fiber composites, foams, sandwich structures, lattice structures, etc. As mentioned in [33], the choice of the components and their volume fractions are important parameters to consider when designing architectured materials. Choosing their shape and how they are placed and connected is also necessary. The length scale of the structural unit is also a variable of the architectured design.

Architectured materials comprise microstructures (patterns) smaller than the overall component size. These patterns should be homogeneous in their spatial distribution [34]. Architectured materials can be modeled using a homogenization technique that replaces the architectured material with an equivalent material whose properties are homogenized according to the geometry of each component that makes up the architectured material. In this study, this strategy is used to propose a new fictitious material having $\frac{E}{\rho}$ equal to that of the ice.

4.3. Application: Titanium plate with piezoelectric elements

Different architectures of the substrate can be studied to evaluate the effect of its topology on the E/ρ ratio. In this study, a titanium substrate is considered. As mentioned before, the approach is to couple the titanium sample with a material that has a lower E/ρ ratio. Given the map of material characteristics presented in figure 6, the titanium can be coupled with piezoelectric transducers that are glued to the primary surface, thus creating an additional thickness. Piezoelectric transducers are selected since they can also be used as actuators for de-icing purposes. For the first study, the substrate is defined as a multilayered material with the piezoelectric transducer covering the entire length of the plate $L_{PZT} = L_{Plt} = L$ (Figure 8(a)). This configuration can be seen as a continuous pattern, and it allows the study of the thickness of the piezoelectric transducer required to limit parasitic flexion. Subsequently, it is possible to evaluate a partially multilayered configuration, in which the thickness of the transducer is fixed, while its width is variable (Figure 8(b)).

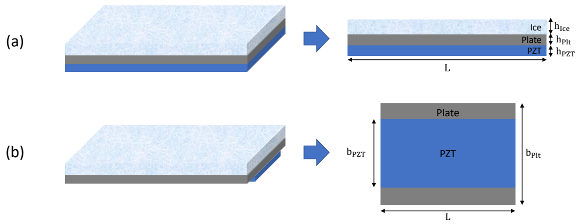

Figure 8: Multilayered material geometry.

4.3.1. First configuration: multilayered material

The multilayered configuration allows analytical calculations. This study aims to determine the transducer thickness for this plate geometry that minimizes the parasitic flexural ratio, regardless of the ice thickness.

Analytical approach. It is possible to calculate the E/ρ ratio from the stiffness K and the mass M of a beam portion.

$$M = \rho A L \tag{27}$$

$$K = \frac{EA}{L} \tag{28}$$

where A is the area of the section, L is the length of the beam, E is the Young's modulus and ρ is the density of the material. Hence, the ratio between Young's modulus and density can be expressed as:

$$\frac{E}{\rho} = \frac{KL^2}{M} \tag{29}$$

Generally, it is possible to adopt this formula to compute the equivalent properties of any architecture. The equivalent stiffness and mass of the model can be retrieved numerically, and the E/ρ ratio can be obtained.

In the multilayered case, since $L_{PZT} = L_{Plt} = L$, the homogenization can be determined analytically. Using equation 29, the equivalent ratio between Young's modulus and density can be expressed as:

$$\left(\frac{E}{\rho}\right)_{eq} = \frac{K_{eq}L^2}{M_{eq}} \tag{30}$$

with :

$$K_{eq} = K_{Plt} + K_{PZT} \tag{31}$$

$$M_{eq} = M_{Plt} + M_{PZT} \tag{32}$$

In this configuration, the ratio between the thickness of the substrate (h_{Plt}) and that of the piezoelectric transducer (h_{PZT}) can be obtained:

$$\frac{h_{Plt}}{h_{PZT}} = \frac{E_{PZT} - \left(\frac{E}{\rho}\right)_{eq}\rho_{PZT}}{\left(\frac{E}{\rho}\right)_{eq}\rho_{Plt} - E_{Plt}} \tag{33}$$

From this equation, it is possible to compute the required thickness of the piezoelectric transducer h_{PZT} to obtain a given $\left(\frac{E}{\rho}\right)_{eq}$ (Table 4).

Numerical approach. The numerical analysis is performed on a titanium plate ($130\times70\times1$ mm^3) covered with ice on one side, and a piezoceramic transducer that covers the entire plate is attached to its other side. Three piezoelectric materials (PIC 151, PIC 181, and PIC 255) are evaluated, and their properties are reported in table 3. The plate is tested in free boundary conditions.

Table 3: Material parameters of the studied piezoceramic transducers

Material parameters	PIC181	PIC151	PIC255
$\rho(kg/m^3)$	7850	7800	7800
ϵ_{11}^S	740	1110	930
ϵ_{33}^S	624	852	887
$e_{31}(N/Vm)$	-4.5	-9.6	-7.15
$e_{33}(N/Vm)$	14.7	15.1	13.7
$e_{15}(N/Vm)$	11	12	11.9
$c_{11}^E(N/m^2)$	152.3E9	107.6E9	123E9
$c_{12}^E(N/m^2)$	89.09E9	63.12E9	76.7E9
$c_{13}^E(N/m^2)$	85.47E9	63.85E9	70.25E9
$c_{33}^E(N/m^2)$	134.1E9	100.4E9	97.11E9
$c_{44}^E(N/m^2)$	28.3E9	19.62E9	22.26E9
$c_{55}^E(N/m^2)$	28.3E9	19.62E9	22.26E9
$c_{66}^E(N/m^2)$	31.61E9	22.4E9	23.15E9

Figure 9 shows the parasitic flexural ratio for different piezoelectric materials and ice thicknesses. Note that the zone highlighted in lighter blue on the plots indicates the optimal range, where the parasitic flexural ratio is minimized for any ice thickness ranging from 2 to 5 mm. The plots can then be used to determine the optimal piezoelectric thickness for the chosen substrate geometry. Table 4 summarizes the optimal thickness ranges obtained from FEM computations for the three piezoelectric materials. This table also provides, for comparison, the thicknesses calculated using the analytical equation 33. The Young's modulus of the piezoelectric materials used for this calculation was approximated by assuming negligible stress in the third direction and a Poisson's ratio between axis 1 and axis 2 similar to that of the titanium substrate to finally have $E_{tot} = C_{11} - \frac{C_{13}^2}{C_{33}} - \nu C_{12}$. The calculation interval is obtained by using E/ρ ratios of ice between 1 and 1.5 to consider different kinds of ice (from glaze to rime). The range of thicknesses obtained analytically provides preliminary knowledge on the necessary piezoelectric thickness. However, for higher accuracy, numerical analysis is required.

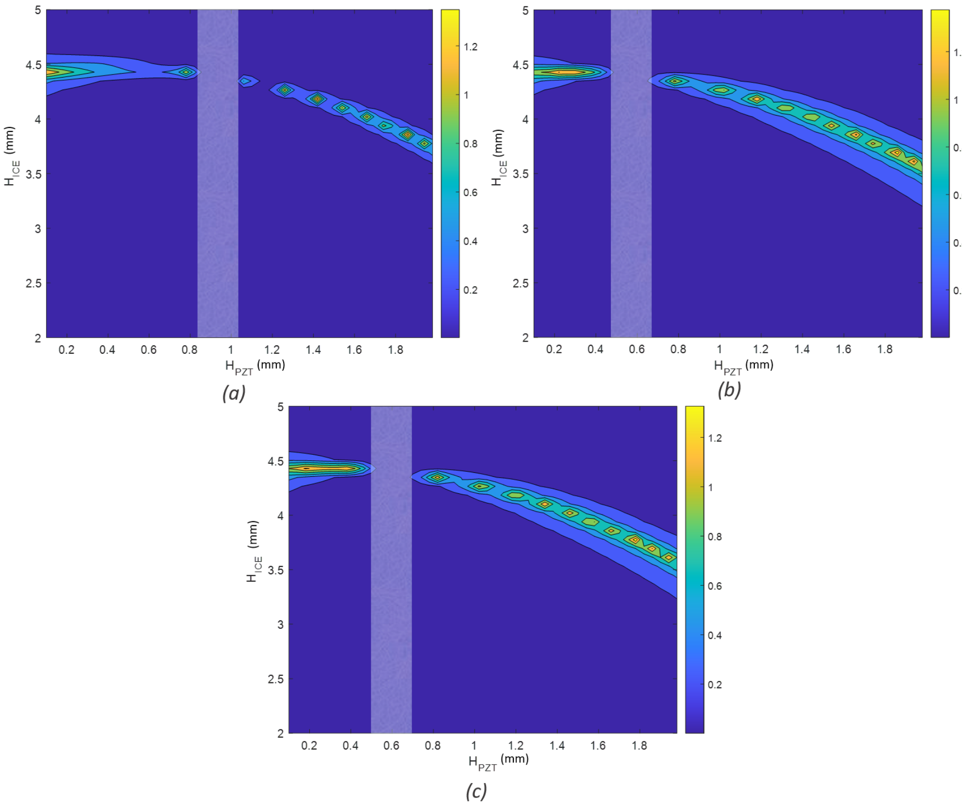

(a) (b) (c)

Figure 9: Numerical calculation of the parasitic flexural ratios as a function of piezoelectric (PZT) transducer and ice thicknesses using (a) PIC181, (b) PIC151, (c) PIC255.

Table 4: Optimal piezoelectric transducer thickness

	PIC181	PIC151	PIC255
FEM optimal thickness (mm)	$[0.85; 1.05]$	$[0.45; 0.7]$	$[0.5; 0.7]$
Analytical optimal thickness (mm)	$[0.46; 3.36]$	$[0.33; 1.37]$	$[0.33; 1.38]$
Equivalent Young's modulus (GPa)	65.7	44.3	44.6

4.3.2. Second configuration: partially multilayered plates

Another potential design approach is establishing a fixed thickness for the piezoelectric transducer and evaluating its width to investigate its impact on the parasitic flexural ratio.

The parasitic flexural ratio is evaluated numerically as the width b_{PZT} of the piezoelectric transducer is varied. A soft piezoelectric transducer having a thickness of $h_{PZT} = 0.5$ mm is adopted. As illustrated in figure 10, the transducer must cover at least 68% of the titanium surface area to obtain a parasitic flexural ratio less than 0.4. Below this value, the extensional mode of the structure may be polluted by parasitic flexion.

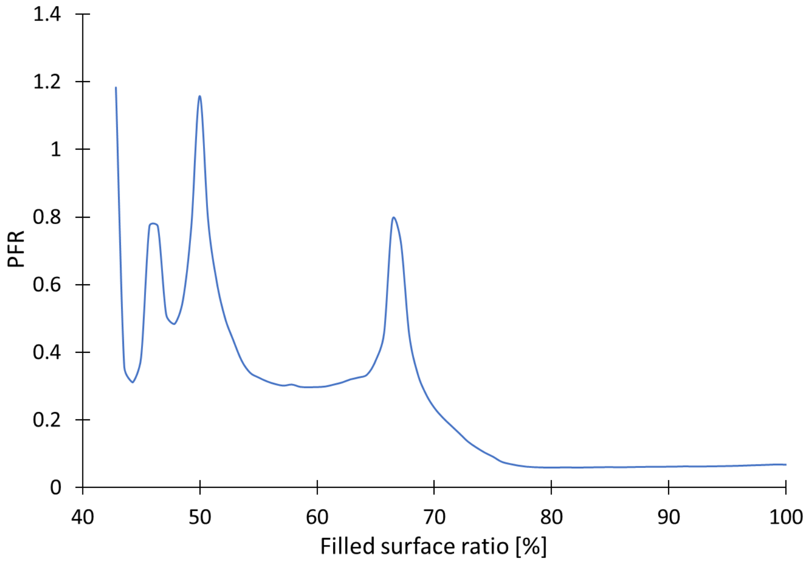

Figure 10: Numerical calculation of the parasitic flexural ratio as a function of the PZT/titanium surface ratio.

5. Prototypes and experimental validations

5.1. Prototypes

To validate the proposed approach, the experimental verification of the previously mentioned designs is proposed. Two titanium prototypes (TA6V) of dimensions 130x70x1 mm^3 were manufactured: a reference plate with two central piezoelectric transducers and a partially multilayered plate. Both plates were equipped with the same 0.5 mm thick soft piezoceramics (PIC 255), available at the time of the tests.

The design of the reference plate is computed considering a pure extensional mode and no parasitic flexion. This results in two piezoelectric transducers located at the center of the plate (see figure 11(a)) to obtain a good coupling between the actuators and the substrate.

The design of the partially multilayered plate is based on the findings presented in 4.3. It results in eight piezoelectric transducers distributed along the plate (see figure 11(b)). While this is an increase in the number of transducers compared to the reference case, the purpose of this investigation is not to optimize the piezoelectric transducers, but to improve the effectiveness of de-icing using extensional modes. Furthermore, to have a direct comparison with the reference plate, only the two central transducers of the partially multilayered configuration will be used for the de-icing tests.

Hereafter, the modal characteristics, parasitic flexural ratios, and de-icing performances of the two prototypes are shown and discussed.

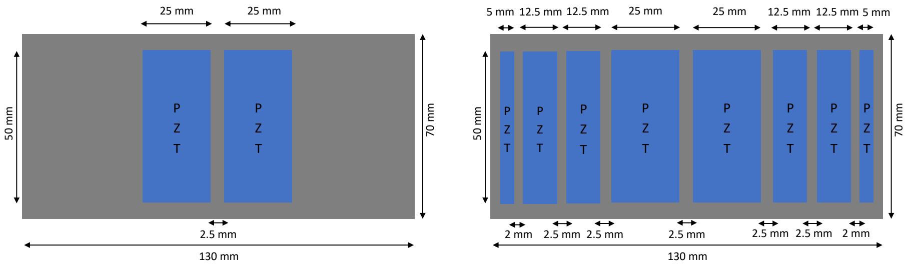

(a) (b)

Figure 11: Bottom view of the two titanium prototypes (130x70x1 mm^3): (a) Reference substrate (b) Partially multilayered substrate.

The considered mode for de-icing is the first mode of extension of the structure, characterized by a frequency ranging from 16 to 17 kHz depending on the ice thickness. The modal shapes of the reference substrate with ice layers of thickness 2, 2.5, 3, 3.5, 4 and 4.5 mm respectively are shown in figure

12. For ice thicknesses of 3 mm, 4 mm and 4.5 mm, the parasitic flexural ratio equals 0.3, 0.15 and 0.13 respectively, which is low enough to get an efficient de-icing with the criterion given in Section 2. However, the parasitic flexural ratio highlights a greater coupling between flexion and extension for 2 mm, 2.5 mm and 3.5 mm of ice, for which the indicator equals 1.26, 1.04 and 0.62 respectively. This means that, for these thicknesses, the de-icing capability using the extensional mode is reduced by the presence of flexion.

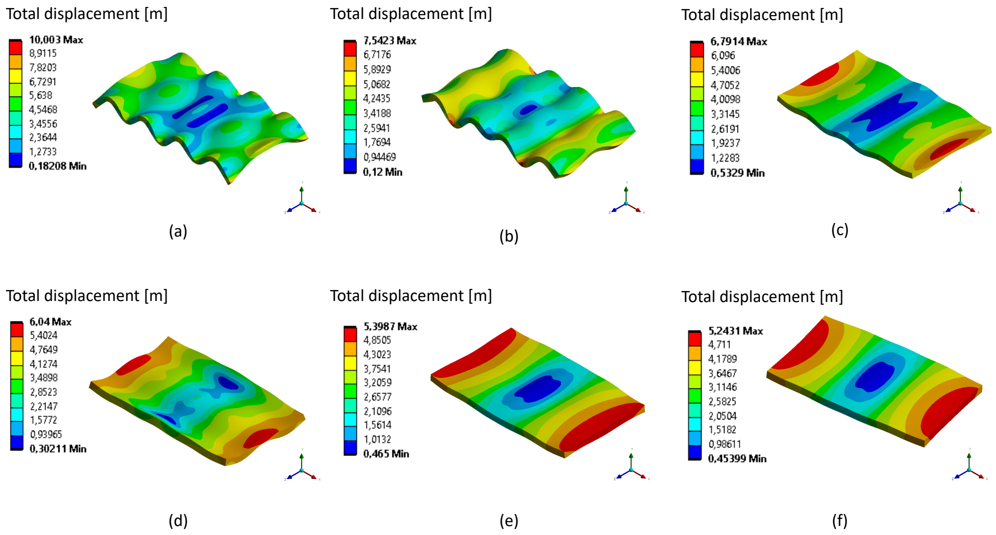

Figure 12: Modal shapes of the extensional mode for the reference substrate with (a) 2 mm of ice (17.7 kHz, PFR = 1.26), (b) 2.5 mm of ice (17.6 kHz, PFR = 1.04), c) 3 mm of ice (17 kHz, PFR = 0.3), (d) 3.5 mm of ice (16.9 kHz, PFR = 0.62), (e) 4 mm of ice and (16.6 kHz, PFR = 0.15), (f) 4.5 mm of ice (16.5 kHz, PFR = 0.13).

Figure 13 shows the modal shapes of the partially multilayered substrate for the same ice thicknesses studied for the reference prototype. The first mode of extension is found at a frequency of around 15 kHz. It is possible to notice that the parasitic flexural ratios are generally lower than those of the reference plate. For 2 mm the value equals 0.57, while for 2.5 mm, 3 mm, 3.5 mm, 4 and 4.5 mm, the parasitic flexural ratio equals 0.33, 0.34, 0.15, 0.11 and 0.15 respectively, thus less than 0.4. Table 5 summarizes the values of the parasitic flexural ratios for both the reference and multilayered plates. From a numerical standpoint, the effect of the partially multilayered configuration is therefore beneficial to the reduction of parasitic flexion.

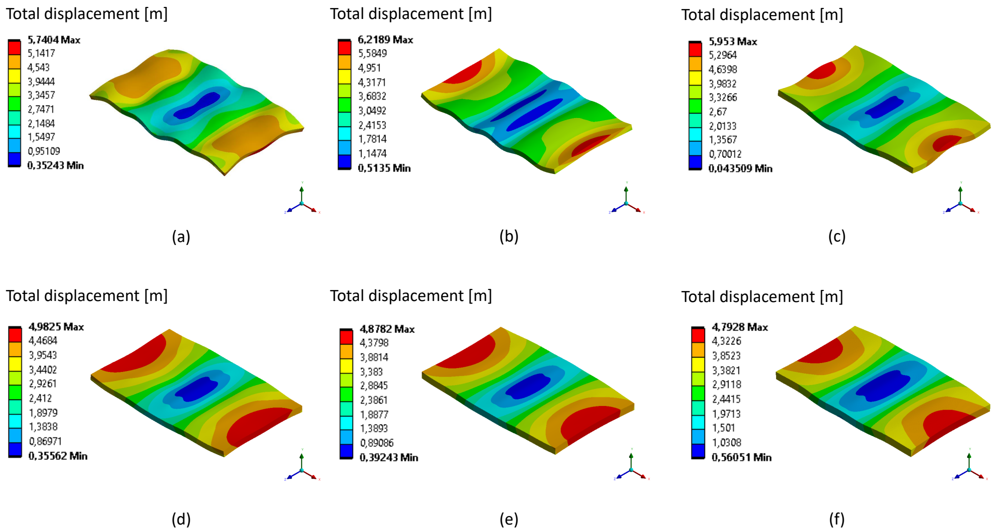

Figure 13: Modal shapes of the extensional mode for the partially multilayered substrate with (a) 2 mm of ice (15.7 kHz, PFR = 0.57), (b) 2.5 mm of ice (15.5 kHz, PFR = 0.33), (c) 3 mm of ice (15.4 kHz, PFR = 0.34), (d) 3.5 mm of ice (15.3 kHz, PFR = 0.15), (e) 4 mm of ice and (15.2 kHz, PFR = 0.11), (f) 4.5 mm of ice (15.1 kHz, PFR = 0.15).

Table 5: Parasitic flexural ratios for different ice thicknesses

h$_{ice}$	2 mm	2.5 mm	3 mm	3.5 mm	4 mm	4.5 mm
PFR (Reference)	1.26	1.04	0.3	0.62	0.15	0.13
PFR (Partially multilayered)	0.57	0.33	0.34	0.15	0.12	0.15

The configuration with 3.5 mm, 4 mm and 4.5 mm of ice were evaluated experimentally. Tests with thinner layers of ice were not possible because the voltage required for de-icing was greater than what the piezoelectric transducers could tolerate. However, the chosen thicknesses allow showing two cases:

- the configurations with 4 mm and 4.5 mm of ice exhibit a minor coupling between extensional and flexural modes. The de-icing should be successful for both prototypes.
- the configuration with 3.5 mm of ice presents an extensional mode strongly coupled with parasitic flexion in the case of the reference prototype (PFR = 0.62). However, coupling is minimal in the case of the partially multilayered substrate. The de-icing should be successful with the partially multilayered substrate, but not with the reference one.

5.2. De-icing tests

The ice is formed in a freezer by spraying demineralized water on the plates. The substrate is pre-cooled at the freezer temperature of -20 °C. An electronic caliper (Mitutoyo Absolute AOS Digimatic) is used to verify that the desired ice thickness is reached. For both prototypes, a preliminary 20Vpk sweep is done to detect the extensional resonant frequency. Then, the de-icing tests are performed at 260Vpk for a total time of 8 s using both central piezoelectric transducers as actuators.

Complete de-icing is achieved for the multilayered plate (figure 14(b)) with 3.5 mm of ice accumulated on the top of the plate. Cohesive cracks form first, followed by adhesive propagation, resulting in a clean surface at the end of de-icing. The de-icing process was completed in 4 s. The reference plate (figure 14(a)) experienced cohesive cracks as well as adhesive propagation for the same ice thickness, but the latter was not sufficient to shed the ice layer, which was still bonded at the end of the test. Similar results were also found for lower voltages (200Vpk) [2]. For ice thicknesses of 4 mm and 4.5 mm, the de-icing is effective for both prototypes (see figures 15, 16). The results are in good agreement with the numerical analyses. The partially multilayered plate can effectively de-ice all tested ice thicknesses, while the reference plate experiences some configurations where the de-icing is unsuccessful due to parasitic flexion.

---

[2] All videos are available in the supplementary contents

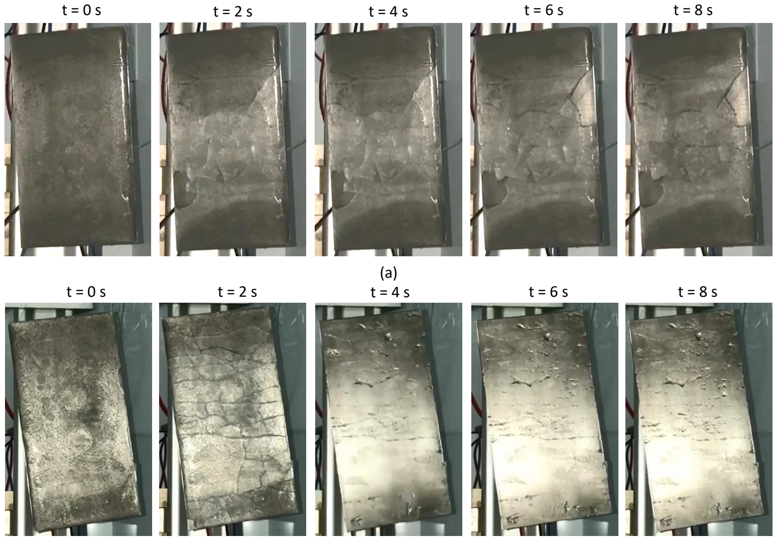

(a)

(b)

Figure 14: 260Vpk extensional de-icing of a 3.5 mm thick ice layer: a) Reference substrate (b) Partially multilayered substrate.

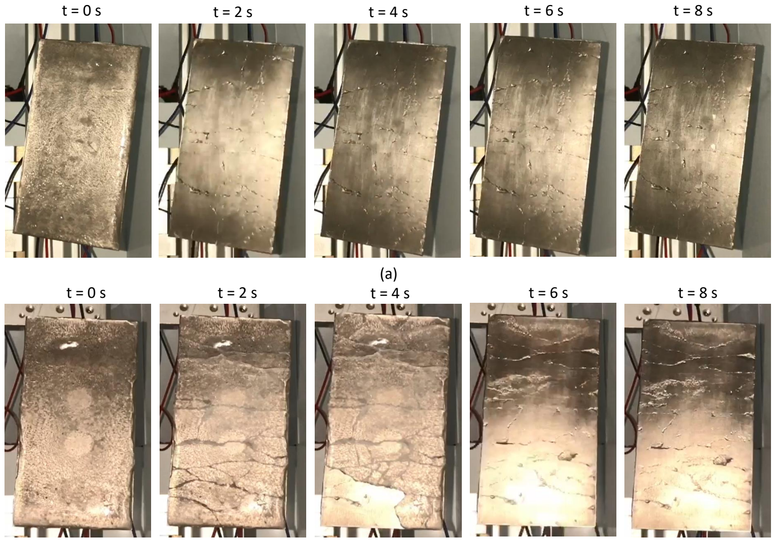

(a)

(b)

Figure 15: 260Vpk extensional de-icing of a 4 mm thick ice layer: a) Reference substrate (b) Partially multilayered substrate.

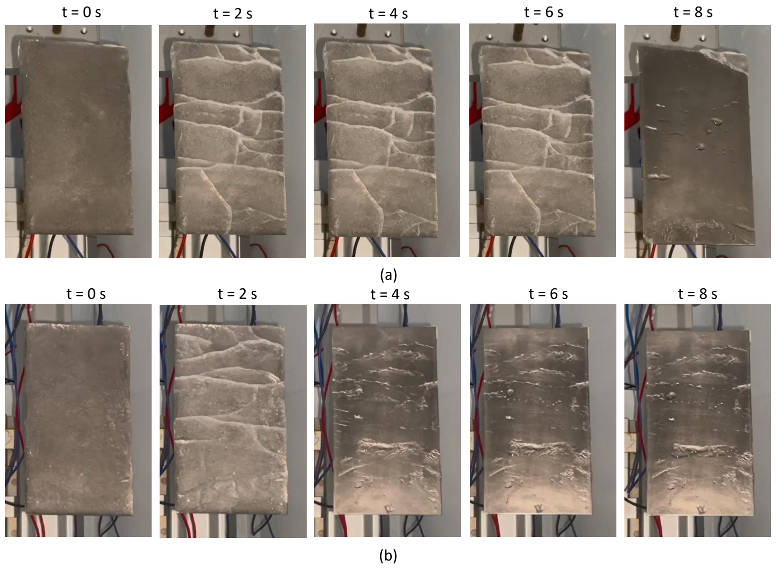

Figure 16: 260Vpk extensional de-icing of a 4.5 mm thick ice layer: a) Reference substrate (b) Partially multilayered substrate.

6. Conclusion

This paper proposes design guidelines for an effective ultrasonic de-icing system based on piezoelectric transducers and using an extensional resonant mode. The preliminary numerical study shows that strong coupling of the extensional mode with flexion can negatively impact the resonant mode's ability to shed ice. Therefore, selecting extensional modes with low parasitic flexion is a criterion to achieve effective de-icing. The analytical demonstration of the coupled wave equations has shown that the E/ρ ratio of the substrate should be as close as possible to that of the ice to ensure a pure extensional mode. However, this is not possible using conventional, single-layered substrates. Hence, a methodology based on multilayered materials is proposed, which consists of creating a new fictitious material by combining two or more constitutive materials.

A reference prototype and a partially multilayered prototype of a titanium plate were studied numerically. The parasitic flexural ratio, which quantifies the amount of flexion in the studied extensional mode, was computed for different ice thicknesses. It was found that the partially multilayered architecture ensured lower ratios for all ice thicknesses, while the reference plate exhibited high values of parasitic flexion for certain ice thicknesses.

Finally, the partially multilayered architectured substrate was tested and compared to the non-optimized reference for three different ice thicknesses. The results showed that, for a 3.5 mm thick ice layer, the de-icing was successful when the first extensional mode of the partially multilayered plate was excited, while the ice remained attached to the non-optimized plate due to the significant parasitic flexural effects. For the other tested ice thicknesses (4 mm and 4.5 mm), de-icing was successful on both prototypes. All the experimental results were in agreement with the corresponding numerical analyses, allowing the correlation of the value of the parasitic flexural ratio with the de-icing effectiveness. Therefore, the proposed methodology for the design of multilayered materials successfully reduces the effects of parasitic flexion on extensional modes and allows full instantaneous de-icing using extensional modes.

This theoretical work focused on simple structures to enable analytical calculations and understanding of the origin and effects of parasitic flexion when using extensional modes for de-icing. Future developments will involve applying the acquired knowledge to optimize the design of a leading edge equipped with piezoelectric transducers.

7. Acknowledgments

This project has received funding from the European Union's Horizon 2020 research and innovation programme under the Marie Skłodowska-Curie grant agreement No 956703 (SURFICE Smart surface design for efficient ice protection and control).

References

[1] T. Laakso, H. Holttinen, G. Ronsten, L. Tallhaug, R. Horbaty, I. Baring-Gould, A. Lacroix, E. Peltola, B. Tammelin, State-of-the-art of wind energy in cold climates, IEA annex XIX 24 (2003) 53.

[2] J.-L. Laforte, M. Allaire, J. Laflamme, State-of-the-art on power line de-icing, Atmospheric Research 46 (1-2) (1998) 143–158.

[3] R. W. Gent, N. P. Dart, J. T. Cansdale, Aircraft icing, Philosophical Transactions of the Royal Society of London. Series A: Mathematical, Physical and Engineering Sciences 358 (1776) (2000) 2873–2911.

[4] O. Parent, A. Ilinca, Anti-icing and de-icing techniques for wind turbines: Critical review, Cold regions science and technology 65 (1) (2011) 88–96.

[5] F. T. Lynch, A. Khodadoust, Effects of ice accretions on aircraft aerodynamics, Progress in Aerospace Sciences 37 (8) (2001) 669–767.

[6] Y. Cao, W. Tan, Z. Wu, Aircraft icing: An ongoing threat to aviation safety, Aerospace science and technology 75 (2018) 353–385.

[7] V. Vercillo, N. Karpen, A. Laroche, J. A. M. Guillén, S. Tonnicchia, R. de Andrade Jorge, E. Bonaccurso, Analysis and modelling of icing of air intake protection grids of aircraft engines, Cold Regions Science and Technology 160 (2019) 265–272.

[8] O. Meier, D. Scholz, A handbook method for the estimation of power requirements for electrical de-icing systems, DLRK, Hamburg 31 (2010).

[9] C. A. Martin, J. C. Putt, Advanced pneumatic impulse ice protection system (piip) for aircraft, Journal of Aircraft 29 (4) (1992) 714–716.

[10] O. Fakorede, Z. Feger, H. Ibrahim, A. Ilinca, J. Perron, C. Masson, Ice protection systems for wind turbines in cold climate: characteristics, comparisons and analysis, Renewable and Sustainable Energy Reviews 65 (2016) 662–675.

[11] T. Bai, C. Zhu, B. Miao, K. Li, C. Zhu, Vibration de-icing method with piezoelectric actuators, Journal of Vibroengineering 17 (1) (2015) 61–73.

[12] E. Villeneuve, D. Harvey, D. Zimcik, R. Aubert, J. Perron, Piezoelectric deicing system for rotorcraft, Journal of the American Helicopter Society 60 (4) (2015) 1–12.

[13] S. V. Venna, Y.-J. Lin, G. Botura, Piezoelectric transducer actuated leading edge de-icing with simultaneous shear and impulse forces, Journal of Aircraft 44 (2) (2007) 509–515.

[14] E. Villeneuve, C. Volat, S. Ghinet, Numerical and experimental investigation of the design of a piezoelectric de-icing system for small rotorcraft part 3/3: Numerical model and experimental validation of vibration-based de-icing of a flat plate structure, Aerospace 7 (5) (2020) 54.

[15] Z. Wang, Recent progress on ultrasonic de-icing technique used for wind power generation, high-voltage transmission line and aircraft, Energy and Buildings 140 (2017) 42–49.

[16] S. Ramanathan, V. V. Varadan, V. K. Varadan, Deicing of helicopter blades using piezoelectric actuators, in: Smart Structures and Materials 2000: Smart Electronics and MEMS, Vol. 3990, International Society for Optics and Photonics, 2000, pp. 281–292.

[17] C. Yin, Z. Zhang, Z. Wang, H. Guo, Numerical simulation and experimental validation of ultrasonic de-icing system for wind turbine blade, Applied Acoustics 114 (2016) 19–26.

[18] J. Palacios, E. Smith, J. Rose, R. Royer, Instantaneous de-icing of freezer ice via ultrasonic actuation, AIAA journal 49 (6) (2011) 1158–1167.

[19] J. Palacios, E. Smith, J. Rose, R. Royer, Ultrasonic de-icing of wind-tunnel impact icing, Journal of Aircraft 48 (3) (2011) 1020–1027.

[20] A. Overmeyer, J. Palacios, E. Smith, Ultrasonic de-icing bondline design and rotor ice testing, AIAA journal 51 (12) (2013) 2965–2976.

[21] D. Li, Z. Chen, Experimental study on instantaneously shedding frozen water droplets from cold vertical surface by ultrasonic vibration, Experimental thermal and fluid science 53 (2014) 17–25.

[22] V. Pommier-Budinger, M. Budinger, P. Rouset, F. Dezitter, F. Huet,

M. Wetterwald, E. Bonaccurso, Electromechanical resonant ice protection systems: initiation of fractures with piezoelectric actuators, AIAA Journal 56 (11) (2018) 4400–4411.

[23] M. Budinger, V. Pommier-Budinger, A. Reysset, V. Palanque, Electromechanical resonant ice protection systems: energetic and power considerations, AIAA Journal 59 (7) (2021) 2590–2602.

[24] V. Palanque, T. Planès, V. Pommier-Budinger, M. Budinger, S. Delbecq, Piezoelectric resonant ice protection systems - part 2/2: Evaluation of the benefits at the aircraft level, Chinese Journal of Aeronautics (2024).

[25] M. Budinger, V. Pommier-Budinger, L. Bennani, P. Rouset, E. Bonaccurso, F. Dezitter, Electromechanical resonant ice protection systems: analysis of fracture propagation mechanisms, AIAA Journal 56 (11) (2018) 4412–4422.

[26] J. Petrovic, Review mechanical properties of ice and snow, Journal of materials science 38 (2003) 1–6.

[27] V. Palanque, E. Villeneuve, M. Budinger, V. Pommier-Budinger, G. Momen, Cohesive strength and fracture toughness of atmospheric ice, Cold Regions Science and Technology 204 (2022) 103679.

[28] E. Villeneuve, S. Ghinet, C. Volat, Experimental study of a piezoelec-

tric de-icing system implemented to rotorcraft blades, Applied Sciences 11 (21) (2021) 9869.

[29] G. Gastaldo, V. Palanque, M. Budinger, V. Pommier-Budinger, Stress and energy release rate influence on ice shedding with resonant electromechanical de-icing systems, in: ICAS 2022-33rd Congress of the International Council of the Aeronautical Sciences, 2022.

[30] W. Weaver Jr, S. P. Timoshenko, D. H. Young, Vibration problems in engineering, John Wiley & Sons, 1991.

[31] V. Palanque, E. Villeneuve, M. Budinger, V. Pommier-Budinger, G. Momen, Experimental measurement and expression of atmospheric ice young's modulus according to its density, Cold Regions Science and Technology 212 (2023) 103890.

[32] F.-X. Kromm, J.-M. Quenisset, R. Harry, T. Lorriot, An example of multimaterials design, Advanced Engineering Materials 4 (6) (2002) 371–374.

[33] M. Ashby, Designing architectured materials, Scripta Materialia 68 (1) (2013) 4–7.

[34] Y. Brechet, J. D. Embury, Architectured materials: Expanding materials space, Scripta Materialia 68 (1) (2013) 1–3.